ARTICLE

doi:10.1038/nature14469

Resonant interactions and chaotic rotation of Pluto's small moons

M. R. Showalter[1] & D. P. Hamilton[2]

Four small moons—Styx, Nix, Kerberos and Hydra—follow near-circular, near-equatorial orbits around the central 'binary planet' comprising Pluto and its large moon, Charon. New observational details of the system have emerged following the discoveries of Kerberos and Styx. Here we report that Styx, Nix and Hydra are tied together by a three-body resonance, which is reminiscent of the Laplace resonance linking Jupiter's moons Io, Europa and Ganymede. Perturbations by the other bodies, however, inject chaos into this otherwise stable configuration. Nix and Hydra have bright surfaces similar to that of Charon. Kerberos may be much darker, raising questions about how a heterogeneous satellite system might have formed. Nix and Hydra rotate chaotically, driven by the large torques of the Pluto–Charon binary.

Pluto's moon Kerberos (previously designated S/2011 (134340)1 or, colloquially, P4) was discovered in 2011[1] using images from the Hubble Space Telescope (HST). It orbits between the paths of Nix and Hydra, which were discovered in 2005 and confirmed in 2006[2]. Follow-up observations in 2012 led to the discovery of the still smaller moon Styx (S/2012 (134340)1 or P5)[3]. The complete data set includes numerous additional detections of both objects from 2010–2012[4–6], plus a few detections from 2005 (H. A. Weaver, personal communication, 2011) and from 2006[7]; see Supplementary Table 1. Figure 1 shows samples of the available images. Motivated by these discoveries, we investigate the dynamics and physical properties of Pluto's four small outer moons.

Orbits

Pluto and Charon comprise a 'binary planet'—two bodies, similar in size, orbiting their common barycentre. Their mutual motion creates a time-variable and distinctly asymmetric gravity field. This induces wobbles in the orbits of the outer moons and also drives much slower apsidal precession and nodal regression[8]. In our analysis, we ignore the short-term wobbles and derive time-averaged orbital elements. This is equivalent to replacing the gravity field by that of two concentric rings containing the masses of Pluto or Charon, each with a radius equal to that body's distance from the barycentre.

We have modelled the orbits using six Keplerian orbital elements (semimajor axis a, eccentricity e, inclination i, mean longitude at epoch λ_0, longitude of pericentre ϖ_0, and ascending node Ω_0) plus three associated frequencies (mean motion n, nodal precession rate $\dot{\varpi}$, and apsidal regression rate $\dot{\Omega}$). We work in the inertial Pluto–Charon (P–C) coordinate frame, with Pluto and Charon in the x–y plane and the z axis parallel to the system's angular momentum pole (right ascension 8 h 52 min 5.5 s, declination -6.218°)[6]. We have solved for these elements and frequencies under a variety of assumptions about how they are coupled (Extended Data Table 1). Table 1 lists the most robustly determined elements, in which we enforce a relationship that ensures $\dot{\varpi} \approx -\dot{\Omega}$; this allows us to fit eight elements rather than nine. We prefer this solution because root-mean-square (RMS) residuals are nearly the same as for the solution where $\dot{\varpi}$ and $\dot{\Omega}$ are allowed to vary independently. Additional possible couplings, involving a and n as well, markedly increase the residuals for Styx and Nix; this suggests that non-axisymmetric gravitational effects, which are not modelled by our concentric ring approximation, can be important. The statistically significant (P-value $\ll 1\%$) ~100-km residuals of Nix and Hydra (Table 1) match the predicted scale of the un-modelled wobbles[8], and so are to be expected.

Table 1 shows that e and i are distinctly non-zero; this was not apparent in prior work, which employed a different coordinate frame[5] or was based on 200-year averages[6]. Our results describe each moon's motion during 2005–2012 more accurately. Variations in n, e and i are detectable during 2010–2012 (Extended Data Fig. 1), illustrating the mutual perturbations among the moons that have been used to constrain their masses[6].

Search for resonances

Pluto's five moons show a tantalizing orbital configuration: the ratios of their orbital periods are close to 1:3:4:5:6[1,3,5,9]. This configuration is reminiscent of the Laplace resonance at Jupiter, where the moons Io, Europa, and Ganymede have periods in the ratio 1:2:4. Table 1 shows the orbital periods P of the moons relative to that of Charon, confirming the near-integer ratios. However, with measured values for $\dot{\varpi}$ and $\dot{\Omega}$ in addition to n, it becomes possible to search for more complicated types of resonances. A general resonance involves an angle $\Phi = \sum_j \left(p_j\lambda_j + q_j\varpi_j + r_j\Omega_j\right)$ and its time derivative $\dot{\Phi} = \sum_j \left(p_j n_j + q_j\dot{\varpi}_j + r_j\dot{\Omega}_j\right)$. Here, ($p_j$, q_j r_j) are integer coefficients and each subscript j is C, S, N, K or H to identify the associated moon. A resonance is recognized by coefficients that sum to zero and produce a very small value of $\dot{\Phi}$; in addition, the resonant argument Φ usually librates around either 0° or 180°.

Using the orbital elements and their uncertainties tabulated in Table 1, we have performed an exhaustive search for strong resonances in the Pluto system. One dominant three-body resonance was identified: $\Phi = 3\lambda_S - 5\lambda_N + 2\lambda_H \approx 180^\circ$. This defines a ratio of synodic periods: $3S_{NH} = 2S_{SN}$, where the subscripts identify the pair of moons. We find that $\dot{\Phi} = -0.007 \pm 0.001^\circ$ per day and that Φ decreases from 191° to 184° during 2010–2012; this is all consistent with a small libration about 180°. Note that this expression is very similar to that for Jupiter's Laplace resonance,

[1]SETI Institute, 189 Bernardo Avenue, Mountain View, California 94043, USA. [2]Department of Astronomy, University of Maryland, College Park, Maryland 20742, USA.

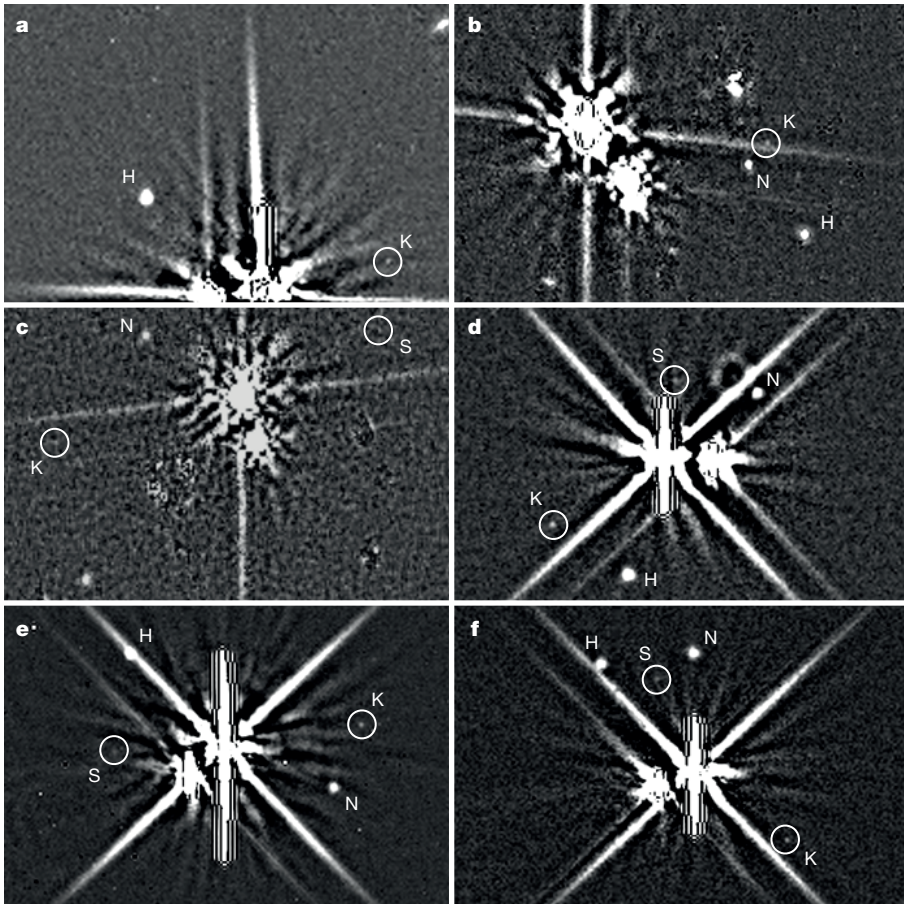

Figure 1 | Example HST images of Pluto's small moons. **a**, Kerberos (K) detected 18 May 2005, in the Nix/Hydra discovery images. **b**, Kerberos in the Nix (N) and Hydra (H) confirmation images of 2 February 2006. **c**, A marginal detection of Styx (S), along with Kerberos, on 2 March 2006. **d**, All four moons, 25 June 2010. **e**, The Kerberos discovery image, 28 June 2011, with Styx also identified. **f**, The Styx discovery image, 7 July 2011. All images were generated by co-adding similar images and then applying an unsharp mask to suppress the glare from Pluto and Charon.

Table 1 | Derived properties of the moons

Property	Styx	Nix	Kerberos	Hydra
a (km)	42,656 ± 78	48,694 ± 3	57,783 ± 19	64,738 ± 3
λ_0 (°)	276.856 ± 0.096	63.866 ± 0.006	94.308 ± 0.021	197.866 ± 0.003
n (° per day)	17.85577 ± 0.00024	14.48422 ± 0.00002	11.19140 ± 0.00005	9.42365 ± 0.00001
e (10^{-3})	5.787 ± 1.144	2.036 ± 0.050	3.280 ± 0.200	5.862 ± 0.025
ϖ_0 (°)	296.1 ± 9.4	221.6 ± 1.4	187.6 ± 3.7	192.2 ± 0.3
$\dot{\varpi}$ (° per day)	0.506 ± 0.014	0.183 ± 0.004	0.115 ± 0.006	0.070 ± 0.001
i (°)	0.809 ± 0.162	0.133 ± 0.008	0.389 ± 0.037	0.242 ± 0.005
Ω_0 (°)	183.4 ± 12.5	3.7 ± 3.4	225.2 ± 5.4	189.7 ± 1.2
$\dot{\Omega}$ (° per day)	−0.492 ± 0.014	−0.181 ± 0.004	−0.114 ± 0.006	−0.069 ± 0.001
P (days)	20.16155 ± 0.00027	24.85463 ± 0.00003	32.16756 ± 0.00014	38.20177 ± 0.00003
P/P_C	3.156542 ± 0.000046	3.891302 ± 0.000004	5.036233 ± 0.000024	5.980963 ± 0.000005
RMS (σ)	1.44	2.59	1.27	2.77
RMS (mas)	17.8	4.22	11.2	3.21
RMS (km)	397	94	248	72
A (km^2)	14 ± 4	470 ± 75	29 ± 8	615 ± 55
R_{100} (km)	2.1 ± 0.3	12.2 ± 1.0	3.0 ± 0.4	14.0 ± 0.6
R_{38} (km)	3.4 ± 0.5	19.8 ± 1.6	4.9 ± 0.7	22.7 ± 1.0
R_{06} (km)	8.6 ± 1.2	50 ± 4	12.4 ± 1.7	57 ± 3
a_{100}/b_{100}		2.1 ± 0.6		1.7 ± 0.6
b_{100}/c_{100}		1.2 ± 0.2		1.2 ± 0.2
ϕ_{2010} (°)		25 ± 10		39 ± 16
ϕ_{2011} (°)		37 ± 15		46 ± 18
ϕ_{2012} (°)		46 ± 17		38 ± 16
V_{100} (km^3)	39 ± 17	5,890 ± 1040	117 ± 49	8,940 ± 1640
GM (10^{-3} km^3 s^{-2})	0.0 + 1.0	3.0 ± 2.7	1.1 ± 0.6	3.2 ± 2.8
Charon-like	**0.018 ± 0.008**	**2.8 ± 0.5**	0.06 ± 0.03	**4.2 ± 0.8**
Bright KBO	**0.04 ± 0.02**	**6.2 ± 1.1**	0.12 ± 0.05	9.4 ± 1.7
Median KBO	**0.12 ± 0.05**	17 ± 3	0.35 ± 0.14	26 ± 5
Dark KBO	**0.26 ± 0.11**	39 ± 7	**0.78 ± 0.32**	60 ± 11

Angles are measured from the ascending node of the P–C orbital plane on the J2000 equator. The epoch is Universal Coordinate Time (UTC) on 1 July 2011. Uncertainties are 1σ. A is disk-integrated reflectivity; R_{100}, R_{38} and R_{06} are radius estimates assuming a spherical shape and p_v = 1, 0.38, and 0.06; V_{100} is the ellipsoidal volume if p_v = 1. Estimates of $GM = G\rho p_v^{-3/2} V_{100}$ are shown for properties resembling those of Charon (density ρ = 1.65 g cm^{-3}; p_v = 0.38) and three types of KBOs: 'bright' (ρ = 0.5; p_v = 0.1), 'median' (ρ = 0.65; p_v = 0.06), and 'dark' (ρ = 0.8; p_v = 0.04). Boldface values are within 1σ of the dynamical mass constraints[6].

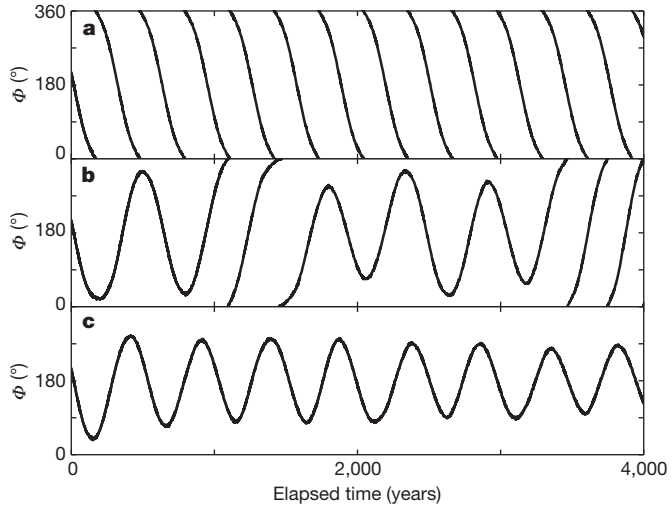

Figure 2 | Numerical integrations of the Styx–Nix–Hydra resonance. Resonant angle Φ is plotted versus time from the current epoch, using three assumptions for GM_H: 0.0032 km^2 s^{-3} (**a**), 0.0039 km^2 s^{-3} (**b**), and 0.0046 km^2 s^{-3} (**c**); these values are equivalent to the nominal mass, a 0.25σ increase, and a 0.5σ increase[6]. GM_N = 0.0044 km^2 s^{-3} throughout, equivalent to 0.5σ above its nominal mass. The modest increase in M_H is sufficient to force a transition of Φ from circulation (Styx outside resonance) to libration (Styx locked in resonance).

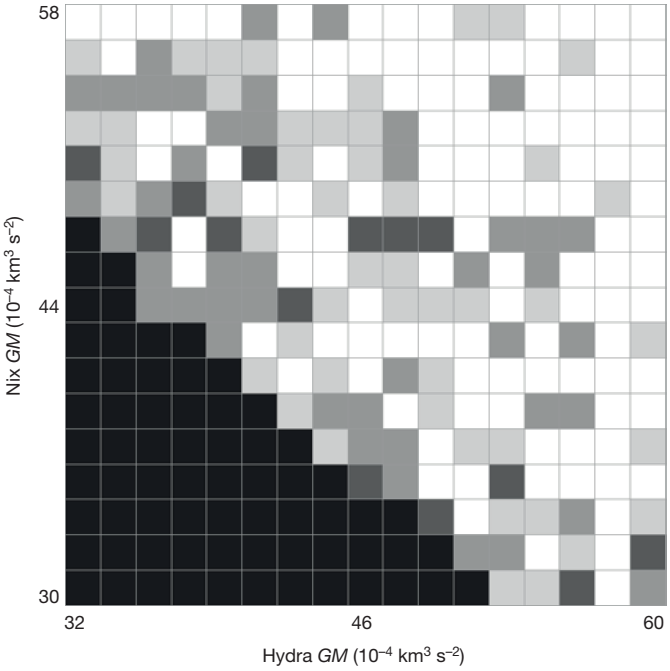

Figure 3 | Mass-dependence of the Laplace-like resonance. The shade of each square indicates whether the associated pair of mass values produces circulation (black) or libration (white) during a 10,000-year integration. The moon masses M_H and M_N are each allowed to vary from nominal to nominal + 1σ (ref. 6). M_K is nominal. Shades of grey define transitional states: light grey if Φ is primarily circulating; dark grey if Φ is primarily librating; medium grey for intermediate states. The transition between black and white is not monotonic, suggesting a fractal boundary.

where $\Phi_L = \lambda_I - 3\lambda_E + 2\lambda_G \approx 180^\circ$ and $2S_{IE} = S_{EG}$. For comparison, Φ_L librates by only ~0.03° (ref. 10). However, a similar resonant angle among the exoplanets of Gliese 876 librates about 0° by ~40° (ref. 11).

Using the current ephemeris and nominal masses[6], our numerical integrations indicate that Φ circulates, meaning that the resonance is inactive (Fig. 2). However, libration occurs if we increase the masses of Nix and Hydra, M_N and M_H, upward by small amounts (Fig. 3). Between these two limits, Φ varies erratically and seemingly chaotically. Extension of Fig. 3 to higher masses reveals that libration is favoured but never guaranteed. By random chance, it would be unlikely to find Styx orbiting so close to a strong three-body resonance, and our finding that $\Phi \approx 180^\circ$ increases the likelihood that this resonance is active. We therefore believe that $M_N + M_H$ has been slightly underestimated. The net change need not be large ($\lesssim 1\sigma$)[6], and is also compatible with the upper limit on $M_N + M_H$ required for the long-term orbital stability of Kerberos[12].

Extended Data Fig. 2 shows that Kerberos contributes to the chaos. To understand its role, we perform simulations in which Pluto and Charon have been merged into one central body, thereby isolating the effects of the other moons on Φ. We perform integrations with M_K = 0 and with M_K nominal, and then Fourier transform $\Phi(t)$ to detect the frequencies of the perturbations (Extended Data Fig. 3). When M_K is non-zero, the power spectrum shows strong harmonics of the three synodic periods S_{SK}, S_{NK} and S_{KH}; this is because $\Phi(t)$ is a linear combination of $\lambda_S(t)$, $\lambda_N(t)$ and $\lambda_H(t)$, and Kerberos perturbs each moon during each passage. The harmonics of a second three-body resonance also appear: $\Phi' = 42\lambda_S - 85\lambda_N + 43\lambda_K \approx 180^\circ$, that is, $42S_{NK} \approx 43S_{SN}$. This was the second strongest resonance found in our search; at the orbit of Styx, the two resonances are separated by just 4 km. This is reminiscent of the Uranus system, where chains of near-resonances drive the chaos in that system[13,14].

These results will influence future models of Pluto system formation. Charon was probably formed by a large impact into Pluto[15], and the outer moons accreted from the leftover debris. If Charon had a large initial eccentricity, then its corotation resonances could lock material into the 1:3:4:5:6 relationship[16]. As Charon's eccentricity damped, the resonant strengths waned, but the moons were left with periods close to these integer ratios[17]. This appealing model has numerous shortcomings, however[18–20]. The presence of a strong Laplace-like resonance places a new constraint on formation models. Additionally, future models must account for the non-zero eccentricities and inclinations of the small satellites; for example, these might imply that the system was excited in the past by resonances that are no longer active[21,22].

The resonance enforces a modified relationship between orbits: if $P_N/P_C = 4$ and $P_H/P_C = 6$, then $P_S/P_C = 36/11 \approx 3.27$. Nevertheless, the other three near-integer ratios remain unlikely to have arisen by chance. Excluding Styx, the probability that three real numbers would all fall within 0.11 of integers is just 1%.

Shapes, sizes and physical properties

Mean disk-integrated photometry for each moon is listed in Table 1. To infer the sizes of these bodies, we also require their visual geometric albedos p_v. Charon is a relatively bright, with $p_v \approx 0.38$. Kuiper Belt objects (KBOs) exhibit a large range of albedos, but the smallest KBOs tend to be dark; $p_v \approx 0.04$–0.08 is common[23–26].

The photometry is expected to vary with phase angle α and, if a body is elongated or has albedo markings, with rotational phase. Extended Data Fig. 4 shows the raw photometry for Nix and Hydra. In spite of the otherwise large variations, an opposition surge is apparent for $\alpha \lesssim 0.5^\circ$; this is often seen in phase curves and is indicative of surface roughness. After dividing out the phase function model, Fig. 4 shows our measurements versus orbital longitude relative to Earth's viewpoint. The measurements of Nix show no obvious pattern, suggesting that it is not in synchronous rotation; this is discussed further below.

With unknown rotation states, we can only assess the light curves in a statistical sense. We proceeded with some simplifying assumptions. (1) Each moon is a uniform triaxial ellipsoid, with dimensions (a_{100}, b_{100}, c_{100}), assuming p_v = 1. (2) Each measurement was taken at a randomly chosen, unknown rotational phase. (3) Each moon was

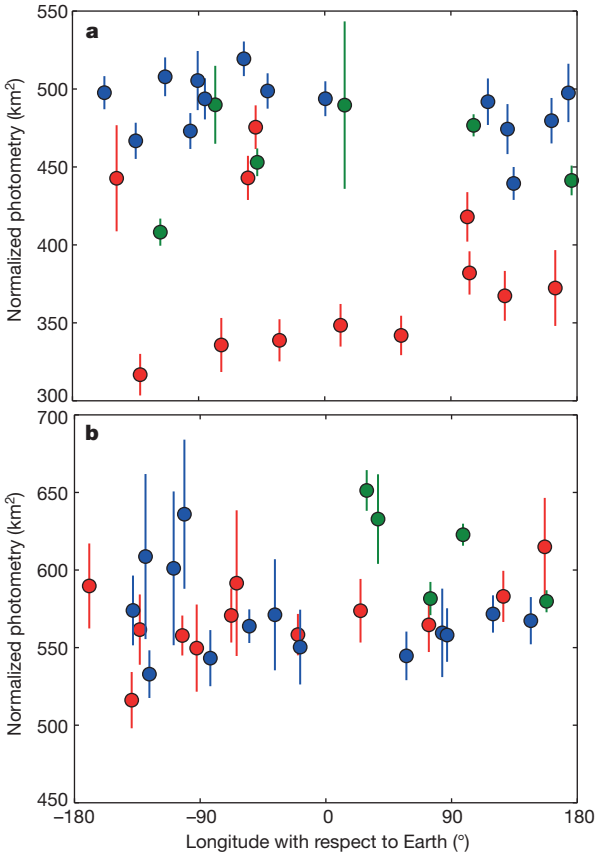

Figure 4 | Normalized light curves. Disk-integrated photometry and 1σ error bars for Nix (**a**) and Hydra (**b**) have been normalized to $\alpha = 1^\circ$ and then plotted as a function of projected orbital longitude. Here 0° corresponds to inferior conjunction with Pluto as seen from Earth. Measurements are colour-coded by year: red for 2010, green for 2011, and blue for 2012. A tidally locked moon would systematically brighten at maximum elongation (90° and 270°).

in fixed rotation about its short axis. (4) The pole orientation may have changed during the gap in coverage between years; this is consistent with Supplementary Video 1, in which the rotation poles are generally stable for months at a time. We therefore describe the orientation by three values of sub-Earth planetocentric latitude: ϕ_{2010}, ϕ_{2011}, and ϕ_{2012}. We used Bayesian analysis to solve for the six parameters that provide the best statistical description of the data; see the Methods section for details.

Nix has an unusually large axial ratio of ~2:1 (Table 1), comparable to that of Saturn's extremely elongated moon, Prometheus. Hydra is also elongated, but probably less so. Also, Nix's year-by-year variations (Fig. 4) are the result of a rotation pole apparently turning towards the line of sight; this explains both its brightening trend and also the decrease in its variations during 2010–2012 (Extended Data Fig. 5). Pluto's sub-Earth latitude is 46°, so Hydra's measured pole is nearly compatible with the system pole. Nix's pole was ~20° misaligned in 2010 but may have reached alignment by 2012.

Given the inferred volume and an assumed albedo and density, we can estimate GM, where M is the mass and G is the gravitation constant. We consider four assumptions about the moons' physical properties, and compare GM to the dynamical estimates[6] (Table 1). Nix and Hydra are probably bright, Charon-like objects; if they were darker, then GM would be too large to be compatible with upper limits on the masses[12].

Kerberos seems to be very different (Table 1). The dynamical inference that its mass is about a third that of Nix and Hydra, yet that it reflects only ~5% as much sunlight, implies that it is very dark. This violates our expectation that the moons should be self-similar due to the ballistic exchange of regolith[27]. Such heterogeneity has one precedent in the Solar System: at Saturn, Aegaeon is very dark ($p_v < 0.15$), unlike any other satellite interior to Titan, and even though it is embedded within the ice-rich G ring[28]. The formation of such a heterogeneous satellite system is difficult to understand. Alternatively, the discrepancy would go away if the estimate of M_K is found to be high by ~2σ; this has a nominal likelihood of <1%. Further study is needed.

Rotation states

Nearly every moon in the Solar System rotates synchronously; the only confirmed exception is Hyperion, which is driven into chaotic rotation by a resonance with Titan[29,30]. Neptune's highly eccentric moon Nereid may also rotate chaotically[31], but observational support is lacking[32,33]. We have searched for rotation periods that are consistent with the light curves of Nix and Hydra (Fig. 4), but results have been negative (Extended Data Fig. 6). Although we can sometimes find a rotation period that fits a single year's data (spanning 2–6 months), no single rotation period is compatible with all three years of data.

Dynamical simulations explain this peculiar result: a binary planet tends to drive its moons into chaotic rotation. This is illustrated in Fig. 5, showing the simulated rotation period and orientation of Nix versus time. The moon has a tendency to lock into near-synchronous rotation for brief periods, but these configurations do not persist. At other times, the moon rotates at a period entirely unrelated to its

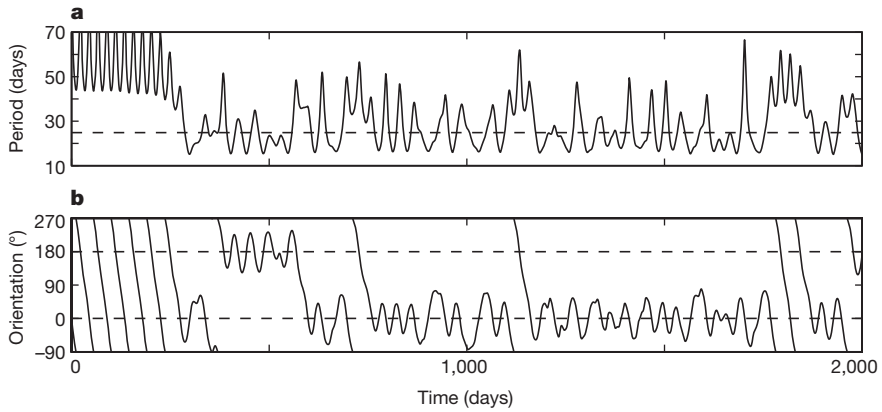

Figure 5 | Numerical simulations of Nix's rotation. **a**, The instantaneous rotation period is compared to the synchronous rate (dashed line). **b**, The orientation is described by the angle between Nix's long axis and the direction towards the barycentre. Nix librates about 0° or 180° for periods of time, but it jumps out of these states frequently.

orbit. Supplementary Video 1 provides further insights into the behaviour; for example, it shows occasional pole flips, a phenomenon consistent with the observed changes in Nix's orientation. Lyapunov times are estimated to be a few months, or just a few multiples of the moons' orbital periods. The timescale of the chaos depends on initial conditions and on assumptions about the axial ratios of the moons. The torques acting on a less-elongated body such as Hydra are weaker, but nevertheless our integrations support chaos.

According to integrations spanning a few centuries, a moon that begins in synchronous rotation will stay there, albeit with large librations. It is therefore possible for synchronous rotation about Pluto and Charon to be stable. However, the large and regular torques of Pluto and Charon probably swamp the small effects of tidal dissipation within the moons, so they never have a pathway to synchronous lock.

Both photometry and dynamical models support the hypothesis that Nix and Hydra are in chaotic rotation. The mechanism is similar to that driving Hyperion's chaos, with Charon playing Titan's role. However, Titan's influence on Hyperion is magnified by a strong orbital resonance. For a binary such as Pluto–Charon, it appears to be a general result that non-spherical moons may rotate chaotically; no resonance is required.

Future observations

The New Horizons spacecraft will fly past Pluto on 14 July 2015. At that time, many of the questions raised by this paper will be addressed. Although Kerberos will not be well resolved (2–3 km per pixel), images will settle the question of whether it is darker than the other moons. The albedos and shapes of Nix (imaged at $\lesssim$0.5 km per pixel) and Hydra (at 1 km per pixel) will be very well determined. New Horizons will not obtain precise masses for the outer moons, but ongoing Earth-based astrometry and dynamical modelling will continue to refine these numbers, while also providing new constraints on the Laplace-like resonance. Because this resonance has a predicted libration period of centuries, the dynamical models will confirm or refute it long before a complete libration or circulation period can be observed.

Chaotic dynamics makes it less likely that we will find rings or additional moons of Pluto. Within the Styx–Hydra region, the only stable orbits are co-orbitals of the known moons. The region beyond Hydra appears to be the region in which it is most likely that we will find additional moons[17], although some orbits close to Pluto are also stable[34]. Independent of the new discoveries in store, we have already learned that Pluto hosts a rich and complex dynamical environment, seemingly out of proportion to its diminutive size.

Online Content Methods, along with any additional Extended Data display items and Source Data, are available in the online version of the paper; references unique to these sections appear only in the online paper.

Received 29 October 2014; accepted 31 March 2015.

1. Showalter, M. R. *et al.* New satellite of (134340) Pluto: S/2011 (134340). *IAU Circ.* **9221** (2011).
2. Weaver, H. *et al.* Discovery of two new satellites of Pluto. *Nature* **439,** 943–945 (2006).
3. Showalter, M. R. *et al.* New satellite of (134340) Pluto: S/2012 (134340). *IAU Circ.* **9253** (2012).
4. Weaver, H. A. *et al.* New satellite of (134340) Pluto: S/2011 (134340). *IAU Circ.* **9221** (2011).
5. Buie, M. W., Grundy, W. M. & Tholen, D. J. Astrometry and orbits of Nix, Kerberos, and Hydra. *Astron. J.* **146,** 152 (2013).
6. Brozović, M., Showalter, M. R., Jacobson, R. A. & Buie, M. W. The orbits and masses of satellites of Pluto. *Icarus* **246,** 317–329 (2015).
7. Steffl, A. J. *et al.* New satellite of (134340) Pluto: S/2011 (134340). *IAU Circ.* **9221** (2011).
8. Lee, M. H. & Peale, S. J. On the orbits and masses of the satellites of the Pluto-Charon system. *Icarus* **184,** 573–583 (2006).
9. Buie, M. W. *et al.* Orbits and photometry of Pluto's satellites: Charon, S/2005 P1, and S/2005 P2. *Astron. J.* **132,** 290–298 (2006).
10. Sinclair, A. T. The orbital resonance amongst the Galilean satellites of Jupiter. *Mon. Not. R. Astron. Soc.* **171,** 59–72 (1975).
11. Rivera, E. J. *et al.* The Lick-Carnegie Exoplanet Survey: a Uranus-mass fourth planet for GJ 876 in an extrasolar Laplace configuration. *Astrophys. J.* **719,** 890–899 (2010).
12. Youdin, A. N., Kratter, K. M. & Kenyon, S. J. Circumbinary chaos: using Pluto's newest moon to constrain the masses of Nix and Hydra. *Astrophys. J.* **755,** 17 (2012).
13. Quillen, A. C. & French, R. S. Resonant chains and three-body resonances in the closely-packed inner Uranian satellite system. *Mon. Not. R. Astron. Soc.* **445,** 3959–3986 (2014).
14. French, R. G., Dawson, R. I. & Showalter, M. R. Resonances, chaos, and short-term interactions among the inner Uranian satellites. *Astron. J.* **149,** 142–169 (2015).
15. Canup, R. M. A giant impact origin of Pluto-Charon. *Science* **307,** 546–550 (2005).
16. Ward, W. R. & Canup, R. M. Forced resonant migration of Pluto's outer satellites by Charon. *Science* **313,** 1107–1109 (2006).
17. Kenyon, S. J. & Bromley, B. C. The formation of Pluto's low-mass satellites. *Astron. J.* **147,** 8–24 (2014).
18. Lithwick, Y. & Wu, Y. The effect of Charon's tidal damping on the orbits of Pluto's three moons. Preprint at http://arxiv.org/abs/0802.2939 (2008).
19. Lithwick, Y. & Wu, Y. On the origin of Pluto's minor moons, Nix and Hydra. Preprint at http://arxiv.org/abs/0802.2951 (2008).
20. Walsh, K. & Levison, H. F. Formation and evolution of Pluto's small satellites. Preprint at http://arxiv.org/abs/1505.01208 (2015).
21. Zhang, K. & Hamilton, D. P. Orbital resonances in the inner Neptunian system I. The 2:1 Proteus-Larissa mean-motion resonance. *Icarus* **188,** 386–399 (2007).
22. Zhang, K. & Hamilton, D. P. Orbital resonances in the inner Neptunian system II. Resonant history of Proteus, Larissa, Galatea, and Despina. *Icarus* **193,** 267–282 (2008).
23. Grundy, W. M., Noll, K. S. & Stephens, D. C. Diverse albedos of small trans-neptunian objects. *Icarus* **176,** 184–191 (2005).
24. Lykawka, P. S. & Mukai, T. Higher albedos and size distribution of large transneptunian objects. *Planet. Space Sci.* **53,** 1319–1330 (2005).
25. Stansberry, J. *et al.* in *The Solar System beyond Neptune* (eds Barucci, M. A. *et al.*) 161–179 (Univ. Arizona Press, 2007).
26. Lacerda, P. *et al.* The albedo–color diversity of transneptunian objects. *Astrophys. J.* **793,** L2 (2014).
27. Stern, S. A. Ejecta exchange and satellite color evolution in the Pluto system, with implications for KBOs and asteroids with satellites. *Icarus* **199,** 571–573 (2009).
28. Hedman, M. M., Burns, J. A., Thomas, P. C., Tiscareno, M. S. & Evans, M. W. Physical properties of the small moon Aegaeon (Saturn LIII). *Eur. Planet. Space Congr. Abstr.* **6,** 531 (2011).
29. Wisdom, J., Peale, S. J. & Mignard, F. The chaotic rotation of Hyperion. *Icarus* **58,** 137–152 (1984).
30. Klavetter, J. J. Rotation of Hyperion. I—Observations. *Astron. J.* **97,** 570–579 (1989).
31. Dobrovolskis, A. R. Chaotic rotation of Nereid? *Icarus* **118,** 181–198 (1995).
32. Buratti, B. J., Gougen, J. D. & Mosher, J. A. No large brightness variations on Nereid. *Icarus* **126,** 225–228 (1997).
33. Grav, T., Holman, M. J. & Kavelaars, J. J. The short rotation period of Nereid. *Astrophys. J.* **591,** L71 (2003).
34. Giuliatti Winter, S. M., Winter, O. C., Vieira Neto, E. & Sfair, R. Stable regions around Pluto. *Mon. Not. R. Astron. Soc.* **430,** 1892–1900 (2013).

Supplementary Information is available in the online version of the paper.

Acknowledgements M.R.S. acknowledges NASA's Outer Planets Research Program for their support through grants NNX12AQ11G and NNX14AO40G. Support for HST programme GO-12436 was provided by NASA through a grant from the Space Telescope Science Institute, which is operated by the Association of Universities for Research in Astronomy, Inc., under NASA contract NAS5-26555. D.P.H. acknowledges NASA Origins Research Program and grant NNX12AI80G.

Author Contributions M.R.S. performed all of the astrometry, photometry, orbit fitting and numerical modelling discussed here. D.P.H. was co-investigator on the Kerberos discovery and has participated in the dynamical interpretations of all the results.

Author Information Reprints and permissions information is available at www.nature.com/reprints. The authors declare no competing financial interests. Readers are welcome to comment on the online version of the paper. Correspondence and requests for materials should be addressed to M.R.S. (mshowalter@seti.org).

METHODS

Data selection and processing. Our data set encompasses all available HST images of the Pluto system during 2006 and 2010–2012, plus Kerberos in 2005. We neglected HST observations from 2002, 2003, and 2007[5,10], because they are of generally lower quality, rendering Kerberos and Styx undetectable. We emphasized long exposures through broad-band filters, although brief exposures of Charon and Pluto provided geometric reference points. Supplementary Table 1 lists the images and bodies measured. We analysed the calibrated ('flt') image files. To detect Kerberos and Styx, it was often necessary to align and co-add multiple images from the same visit; files produced in this manner are listed in the table with a 'coadd' suffix.

We fitted a model point spread function (PSF) to each detectable body. The PSFs were generated using the 'Tiny Tim' software maintained by the Space Telescope Science Institute (STScI)[35,36]. Upon fitting to the image, the centre of the PSF provides the astrometry and the integrated volume under the two-dimensional curve, minus any background offset, is proportional to the disk-integrated photometry. We measured objects in order of decreasing brightness and subtracted each PSF before proceeding; this reduced the effects of glare on fainter objects. Measurements with implausible photometry were rejected; this was generally the result of nearby background stars, cosmic ray hits, or other image flaws. Further details of the analysis are provided elsewhere[6]. Styx photometry (Table 1) might be biased slightly upward by our exclusion of non-detections; however, photometry of the other moons is very robust.

The Pluto–Charon gravity field. We have simplified the central gravity field by taking its time-average. The resulting cylindrically symmetric gravity field can then be expressed using the same expansion in spherical harmonics that is traditionally employed to describe the field of an oblate planet:

$$V(r,\theta,\phi) = -GM/r\left[1-\sum_{m=2}^{\infty} J_m (R/r)^m P_m(\sin\phi)\right] \quad (1)$$

Here (r, θ, ϕ) are polar coordinates, where r is radius and θ and ϕ are longitude and latitude angles, respectively; G is the gravitation constant, M is the body's mass, R is its equatorial radius, P_m is the mth Legendre polynomial, J_m is the mth coefficient in the expansion. The dependence on θ and the odd m-terms in the series vanish by symmetry. The coefficients J_m can be determined by noting that the potential along the axis of the ring simplifies considerably:

$$V(r,\phi=\pi/2) = -GM/r\left[1+(R/r)^2\right]^{-1/2} \quad (2)$$

This can then be compared to the definition of Legendre polynomials:

$$\left(1-2xt+t^2\right)^{-1/2} = \sum_{m=0}^{\infty} t^m P_m(x) \quad (3)$$

Substituting $t = (R/r)$ and evaluating the expression for $x = 0$ yields:

$$V(r,\phi=\pi/2) = -GM/r \sum_{m=0}^{\infty} (R/r)^m P_m(0) \quad (4)$$

Noting that $P_m(1) = 1$ for all m, equations (1) and (4) can only be equal if the coefficients J_m are negatives of the Legendre polynomials evaluated at zero: $J_2 = 1/2$, $J_4 = -3/8$, $J_6 = 5/16$, and so on. Given this sequence of coefficients, we can determine n, $\dot{\varpi}$ and $\dot{\Omega}$ as functions of semimajor axis a:

$$n^2(a) = GM/a^3\left[1-\sum_{m=2}^{\infty}(1+m)J_m(R/a)^m P_m(0)\right] \quad (5a)$$

$$\kappa^2(a) = GM/a^3\left[1-\sum_{m=2}^{\infty}(1-m^2)J_m(R/a)^m P_m(0)\right] \quad (5b)$$

$$\nu^2(a) = GM/a^3\left[1-\sum_{m=2}^{\infty}(1+m)^2 J_m(R/a)^m P_m(0)\right] \quad (5c)$$

Here κ is the epicyclic frequency and $\dot{\nu}$ is the vertical oscillation frequency. It follows that $\dot{\varpi}(a) = n(a) - \kappa(a)$ and $\dot{\Omega}(a) = n(a) - \nu(a)$. In practice, we treated n as the independent variable because it has the strictest observational constraints, and then derived a, $\dot{\varpi}$ and $\dot{\Omega}$ from it.

Orbit fitting. We modelled each orbit as a Keplerian ellipse in the P–C frame, but with additional terms to allow for apsidal precession and nodal regression. Our model is accurate to first order in e and i; any second-order effects can be neglected because they would be minuscule compared to the precision of our measurements.

We also required an estimate for the location of the system barycentre in each set of images. Because HST tracking is extremely precise between consecutive images, the barycentre location was only calculated once per HST orbit. We solved for the barycentre locations first and then held them fixed for subsequent modelling of the orbital elements. Barycentre locations were derived from the astrometry of Pluto, Charon, Nix and Hydra. We locked Pluto and Charon to the latest ephemeris distributed by the Jet Propulsion Laboratory, PLU043[6]. We accounted for the offset between the centre of light and centre of body for Pluto using the latest albedo map[37]. However, because the number of Pluto and Charon measurements is limited, we also allowed Nix and Hydra to contribute to the solution. For each single year 2006–2012, we solved simultaneously for the barycentre location in each image set and also for orbital elements of Nix and Hydra. For the detection of Kerberos in 2005, the only available pointing reference was Hydra, which we derived from PLU043. By allowing many measurements to contribute to our barycentre determinations, we could improve their quality but also limit any bias introduced by shortcomings of our orbit models. The derived uncertainties in the barycentre locations are much smaller than any remaining sources of error.

A nonlinear least-squares fitter identified the best value for each orbital element and also the covariance matrix, from which uncertainties could be derived. However, as noted in Table 1 and Extended Data Table 1, our RMS residuals (equivalent to the square root of χ^2 per degree of freedom) exceed unity. For Styx and Kerberos, marginal detections probably contributed to the excess; for Nix and Hydra, we have identified the source as the un-modelled wobbles in the orbits. All uncertainty estimates have been scaled upward to accommodate these underestimates.

During the orbit fits, we rejected individual points with excessive residuals, based on the assumption that they were misidentifications or the results of poor PSF fits. Extended Data Table 1 lists values for the number of included (M_1) and rejected (M_0) measurements. Rejecting points, however, would bias our uncertainty estimates downward. We compensated by running Monte Carlo simulations in which we generated ($M_0 + M_1$) Gaussian distributed, two-dimensional random variables and then rejected the M_0 that fall furthest from the origin. The standard deviation among the remainder then gave us an estimate of the factor by which we might have inadvertently reduced our error bars. With this procedure, accidentally rejecting a small number of valid measurements would not bias the uncertainties.

We also explored the implications of making various assumptions about how the orbital elements are coupled (Extended Data Table 1). For the purposes of this paper, we have adopted the $N = 8$ solutions in which $\dot{\Omega}$ can be derived from n and $\dot{\varpi}$. This assumption is helpful because, when e and i are small, the frequencies $\dot{\varpi}$ and $\dot{\Omega}$ are especially difficult to measure. By allowing them to be coupled, we obtained more robust results. Nevertheless, our expectation that $\dot{\varpi}$ and $\dot{\Omega}$ should be roughly equal in magnitude but opposite in sign has been well supported by most of our uncoupled, $N = 9$ fits.

Resonance analysis. We have defined a general resonance using a set of integer coefficients (p_j, q_j, r_j). The strength of a resonance is equal to $C(\boldsymbol{p}, \boldsymbol{q}, \boldsymbol{r})\Pi\mu_j\Pi e_j^{|q_j|}\Pi\sin^{|r_j|}(i_j)$, where μ_j is the mass ratio of moon j to the mass of Pluto. The first product $\Pi\mu_j$ excludes the mass of the smallest moon involved, because a resonance can exist even if one moon is a massless test particle. The function C defines a strength factor, but because it has no simple expression, we ignore it in this analysis except to note, qualitatively, that the strongest resonances tend to involve small coefficients and/or small differences between coefficients.

We performed an exhaustive search for all possible resonances involving up to four non-zero coefficients, with $|p_j| \le 300$, $|q_j| \le 4$, and $|r_j| \le 4$. Symmetry dictates that the coefficients sum to zero and that $\sum_j r_j$ must be even[38]. Because Charon follows a circular, equatorial orbit, $q_C = r_C = 0$. We first identified possible resonances by $\dot{\Phi} < 0.1^\circ$ per day, and then followed up by evaluating Φ for each year. Sets of coefficients for which Φ values clustered near 0° or 180° were given preference. We also favoured sets of coefficients that have simple physical interpretations, and where the absolute values were small and/or close to one another.

Orbital integrations. Our orbit simulations employed the numeric integrator SWIFT[39,40]. We used PLU043[6] as our reference ephemeris; it provides state vectors (positions and velocities) for all the bodies in the system versus time. For simplicity, we neglected bodies outside the Pluto system in most integrations. The Sun is the dominant external perturber, shifting the moons by a few tens of kilometres, primarily in longitude, after one Pluto orbit of 248 years; this is <1% of our orbital uncertainties.

Each integration must begin with initial state vectors and masses for each body. However, the state vectors and masses are closely coupled; any change to one mass requires that we adjust all of the state vectors in order to match the observed orbits. Ideally, this would be accomplished by re-fitting to all of the available

astrometry, but that task is beyond the scope of this paper. To simplify the problem, we generated false astrometry derived directly from PLU043, but sampled at the times of all prior HST visits that detected one or more of the four outer moons. Such measurements date back to 11 June 2002[5,6,9]. For each set of assumed masses, we used a nonlinear least-squares fitter to solve for the initial state vectors that optimally matched this astrometry. A similar technique was used to model the effects of moon masses on the chaotic dynamics of the Uranus system[41]. This procedure guarantees that our numeric integrations will match the actual astrometry with reasonable accuracy, regardless of the masses assumed.

For a few numerical experiments, we investigated the consequences of placing Styx exactly into its Laplace-like resonance (Extended Data Figs 2 and 3). We accomplished this by generating a different set of false astrometry, in which the position of Styx was derived from the requirement that $\Phi = 180^\circ$ at all times.

Photometry. Our numerical simulations suggest that typical rotation periods for each moon are comparable to the orbital period, that is, several weeks. Because this timescale is long compared to one or a few of HST's 95-min orbits, we combined measurements obtained from single or adjacent orbits. In Supplementary Table 1, adjacent orbits are indicated by an orbit number of 2 or 3. Our photometry (Fig. 4 and Extended Data Fig. 4) is defined by the mean and standard deviation of all measurements from a single set of orbits.

We considered two simple models for the light curves described as reflectivity A versus time t:

$$A_1(t) = c_0 + c_1 \sin(\omega t) + c_2 \cos(\omega t) \tag{6a}$$

$$A_2(t) = c_0 + c_1 \sin(\omega t) + c_2 \cos(\omega t) + c_3 \sin(2\omega t) + c_4 \cos(2\omega t) \tag{6b}$$

We then sought the frequency ω that minimizes residuals. Given the small number of measurements in individual years, it was inappropriate to attempt more sophisticated models. Results are shown in Extended Data Fig. 6. For the data from 2010, we did identify frequencies where the residuals are especially small, suggesting that we may have identified a rotation rate for that subset of the data. However, in no case does a frequency persist from 2010 to 2012.

Shape modelling. We have described the axial orientation relative to the line of sight using sub-Earth planetocentric latitude ϕ. The hypothetical light curve of an ellipsoid is roughly sinusoidal; its projected cross-section on the sky varies between extremes $A_{\min}$ and $A_{\max}$. If $\phi = 0$, $A_{\min} = \pi bc$ and $A_{\max} = \pi ac$. If $\phi = 90^\circ$, then $A_{\min} = A_{\max} = \pi ab$. More generally

$$A_{\min}(a,b,c,\phi) = \pi b\left(c^2\cos^2\phi + a^2\sin^2\phi\right)^{1/2} \tag{7a}$$

$$A_{\max}(a,b,c,\phi) = \pi a\left(c^2\cos^2\phi + b^2\sin^2\phi\right)^{1/2} \tag{7b}$$

If ϕ is fixed and each measurement was obtained at a uniformly distributed, random rotational phase, then the conditional probability density function for a cross-section A given $A_{\min}$ and $A_{\max}$ is:

$$P(A|A_{\min}, A_{\max}) \propto \left(1 - [(A - A_0)/\Delta A]^2\right)^{-1/2} \tag{8}$$

where $A_0 \equiv (A_{\max} + A_{\min})/2$ and $\Delta A = (A_{\max} - A_{\min})/2$. In reality, each measurement A has an associated uncertainty σ. This has the effect of convolving P with a normal distribution $N(A, \sigma)$, with zero mean and standard deviation σ.

$$P[\sigma](A|A_{\min}, A_{\max}, \sigma) \propto \left(1 - [(A - A_0)/\Delta A]^2\right)^{-1/2} \otimes N(A, \sigma) \tag{9}$$

where the $\otimes$ operator represents convolution.

However, simulations show that ϕ varies due to chaotic rotation driven by the central binary (Supplementary Video 1). To simplify this analysis, we have assumed that ϕ was fixed for the whole of each year during which we obtained data, but that changes may have occurred between years; this is generally consistent with the time spans of our data sets (a few months per year) and the infrequency of large pole changes in the simulations. This leads us to define three unknowns: ϕ_{2010}, ϕ_{2011}, and ϕ_{2012}. Because $A_{\min}$ and $A_{\max}$ depend only on $\sin^2\phi$ and $\cos^2\phi$, we replace the unknowns ϕ by $S \equiv \sin^2\phi$ in our analysis.

We have a vector of independent measurements $\boldsymbol{A} = (A_0, A_1, \ldots)$ and uncertainties $\boldsymbol{\sigma} = (\sigma_0, \sigma_1, \ldots)$, so the joint, conditional probability of obtaining all our measurements is a product:

$$\begin{aligned} &P(\boldsymbol{A}|a,b,c,S_{2010},S_{2011},S_{2012}) \\ &= \Pi P[\sigma_k]\left(A_k|A_{\min}\left(a,b,c,S_{\mathrm{year}(k)}\right), A_{\max}\left(a,b,c,S_{\mathrm{year}(k)}\right)\right) \end{aligned} \tag{10}$$

where year(k) is the year associated with measurement k. Instead, we seek the joint, conditional probability density function $P(a, b, c, S_{2010}, S_{2011}, S_{2012}|\boldsymbol{A})$. This is a problem in Bayesian analysis:

$$\begin{aligned} &P(a,b,c,S_{2010},S_{2011},S_{2012}|\boldsymbol{A}) \\ &= P(\boldsymbol{A}|a,b,c,S_{2010},S_{2011},S_{2012})P(\boldsymbol{A})/P(a,b,c,S_{2010},S_{2011},S_{2012}) \end{aligned} \tag{11}$$

Here $P(\boldsymbol{A})$ and $P(a, b, c, S_{2010}, S_{2011}, S_{2012})$ represent our assumed 'prior probability' distributions for these quantities. We have no prior information about our measurements A_k, so we assume that they are uniformly distributed. The second prior can be broken down as

$$P(a,b,c,S_{2010},S_{2011},S_{2012}) = P(a,b,c)P(S_{2010})P(S_{2011})P(S_{2012}) \tag{12}$$

because orientations are independent of shape and of one another. If the pole in each year is randomly distributed over 4π steradians, then $P(\phi) \propto \cos\phi$ and $P(S) \propto S^{-1/2}$.

We model our prior for the shape as $P(a, b, c) = P_1(u)P_2(v)P_3(w)$, where $u \equiv abc$; $v \equiv a/b$; and $w \equiv b/c$. This states that we will regard the ellipsoid's volume and its two axial ratios as statistically independent. We have assumed that $\log(u)$ is uniformly distributed rather than u itself, which implies $P_1(u) \propto 1/u$. Experience with other irregularly shaped planetary objects suggests that large ratios a/b and b/c are disfavoured, with values rarely exceeding 2. After some experimentation, we adopted $P_2(v) \propto 1/v^3$ and $P_3(w) \propto 1/w^3$. Alternative but similar assumptions had little effect on our results.

The above equations provide a complete solution to the joint probability function $P(a, b, c, S_{2010}, S_{2011}, S_{2012})$. We solved for the complete six-dimensional function, represented as a six-dimensional array. Quantities listed in Table 1 were derived as the mean and standard deviation of P along each of its six axes, with S converted back to ϕ. Extended Data Fig. 5 compares the distribution of measurements by year with the reconstructed probability distributions.

Simulations of rigid body rotation. The orientation of the ellipsoid can be defined by a unit quaternion: $\boldsymbol{q} = [\cos(\theta/2), \sin(\theta/2)\boldsymbol{u}]$ represents a rotation by angle θ about unit axis vector $\boldsymbol{u}$. The time-derivative $\mathrm{d}\boldsymbol{q}/\mathrm{d}t = [0, \boldsymbol{\omega}]\cdot\boldsymbol{q}/2$, where $\boldsymbol{\omega}$ is the spin vector. We used a Bulirsch–Stoer integrator to track $\boldsymbol{q}$, $\mathrm{d}\boldsymbol{q}/\mathrm{d}t$, $\boldsymbol{x}$ and $\mathrm{d}\boldsymbol{x}/\mathrm{d}t$, where $\boldsymbol{x}$ is the position of the ellipsoid relative to the barycentre. The forces and torques acting were defined by Pluto and Charon following fixed circular paths around the barycentre; this motion was pre-defined for the simulations, not integrated numerically. We derived $\mathrm{d}^2\boldsymbol{x}/\mathrm{d}t^2$ from the gravity force of each body on the ellipsoid. We also required the second derivative of $\boldsymbol{q}$: $\mathrm{d}^2\boldsymbol{q}/\mathrm{d}t^2 = [-|\boldsymbol{\omega}|^2/2, \boldsymbol{\alpha}]\cdot\boldsymbol{q}/2$, where $\boldsymbol{\alpha}$ is the time-derivative of $\boldsymbol{\omega}$. We related $\boldsymbol{\alpha}$ to the torque applied by Pluto and Charon on the ellipsoid

$$\tau = 3GM_P\boldsymbol{r}_P \times (I\boldsymbol{r}_P)/|\boldsymbol{r}_P|^5 + 3GM_C\boldsymbol{r}_C \times (I\boldsymbol{r}_C)/|\boldsymbol{r}_C|^5 \tag{13}$$

where $\boldsymbol{r}_k = \boldsymbol{x} - \boldsymbol{x}_k$ is the vector offset from each body centre to the ellipsoid's centre and I is the ellipsoid's moment of inertia tensor. In the internal frame of the ellipsoid, the moment of inertia tensor I_0 is diagonal, with $I_{11} = (M/5)(b^2 + c^2)$, $I_{22} = (M/5)(a^2 + c^2)$, and $I_{33} = (M/5)(a^2 + b^2)$. It is rotated to the system coordinate frame via the rotation matrix R, which can be calculated from $\boldsymbol{q}$: $I = RI_0R^{\mathrm{T}}$. We then solve for $\boldsymbol{\alpha}$ via the relation $\tau = I\boldsymbol{\alpha} + \boldsymbol{\omega} \times I\boldsymbol{\omega}$.

Code availability. Portions of our software are available at https://github.com/seti/pds-tools. We have opted not to release the entire source code because it is built on top of additional large libraries representing decades of development. Instead, we have documented our algorithms with sufficient detail to enable others to reproduce our results.

35. Krist, J. E., Hook, R. N. & Stoehr, F. 20 years of Hubble Space Telescope optical modeling using Tiny Tim. *Proc. SPIE* **8127,** 1–16 (2011).
36. Space Telescope Science Institute. *Observatory Support: Tiny Tim HST PSF Modeling* http://www.stsci.edu/hst/observatory/focus/TinyTim (2011).
37. Buie, M. W. *et al.* Pluto and Charon with the Hubble Space Telescope. II. Resolving changes on Pluto's surface and a map for Charon. *Astron. J.* **139,** 1128–1143 (2010).
38. Hamilton, D. P. A comparison of Lorentz, planetary gravitational, and satellite gravitational resonances. *Icarus* **109,** 221–240 (1994).
39. Levison, H. F. & Duncan, M. J. The long-term dynamical behavior of short-period comets. *Icarus* **108,** 18–36 (1994).
40. Levison, H. F. *SWIFT: A Solar System Integration Software Package* http://www.boulder.swri.edu/~hal/swift.html (2014).
41. French, R. S. & Showalter, M. R. Cupid is doomed: An analysis of the stability of the inner Uranian satellites. *Icarus* **220,** 911–921 (2012).

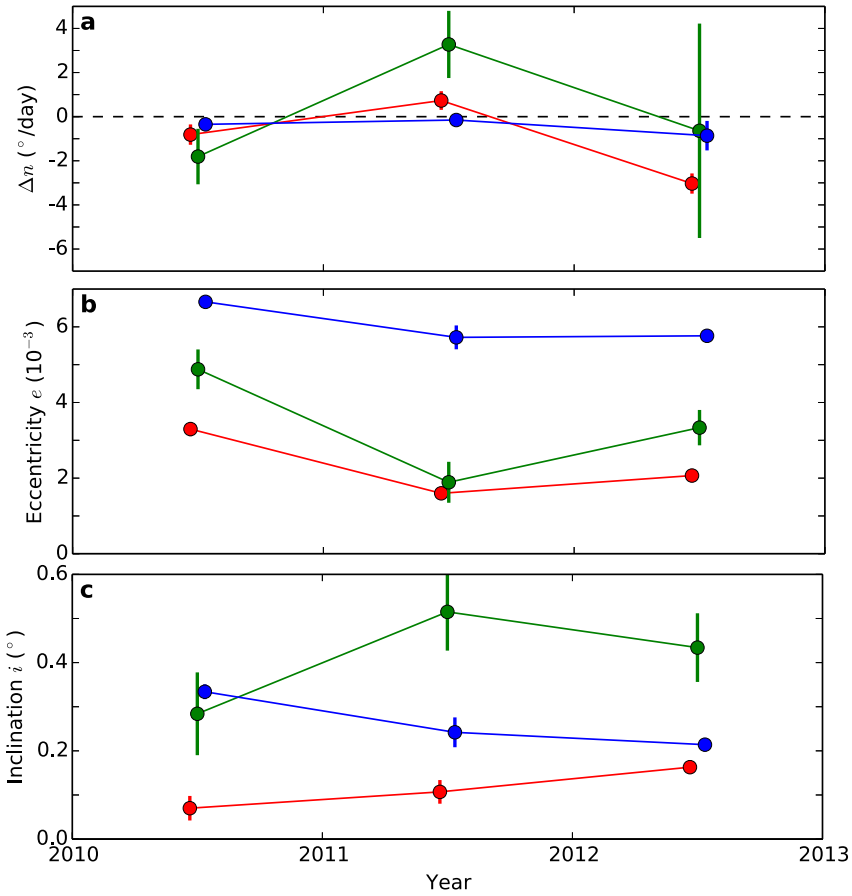

Extended Data Figure 1 | Variations in orbital elements by year. Changes in mean motion (**a**), eccentricity (**b**) and inclination (**c**) are shown during 2010–2012 for Nix (red), Kerberos (green) and Hydra (blue). Vertical bars are $\pm 1\sigma$. Each individual point is a fit to a single year of data (compare with Extended Data Table 1). In **a**, Δn is the mean motion of each body minus its average during 2006–2012.

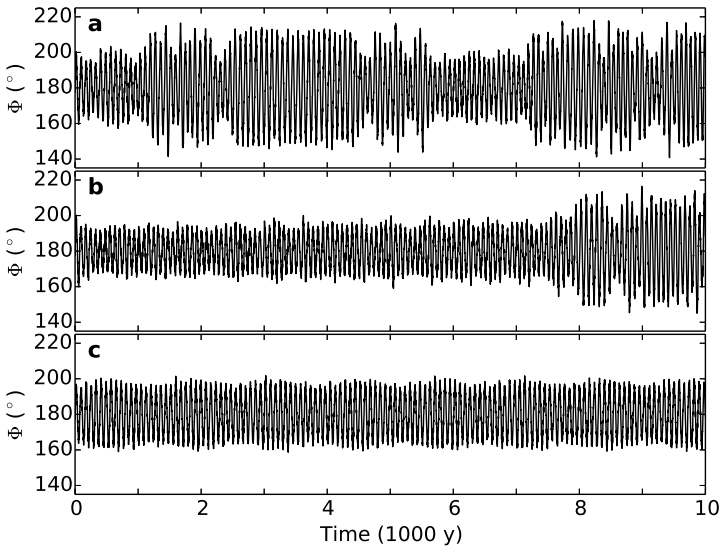

Extended Data Figure 2 | The role of Kerberos in the Laplace-like resonance. We have initiated an integration with Styx exactly in its resonance with Nix and Hydra, and then have allowed it to evolve for 10,000 years. The diagrams are for M_K nominal (**a**), M_K reduced by 1σ (**b**) and $M_K = 0$ (**c**). The amplitude of the libration is stable when Kerberos is massless, but shows erratic variations otherwise.

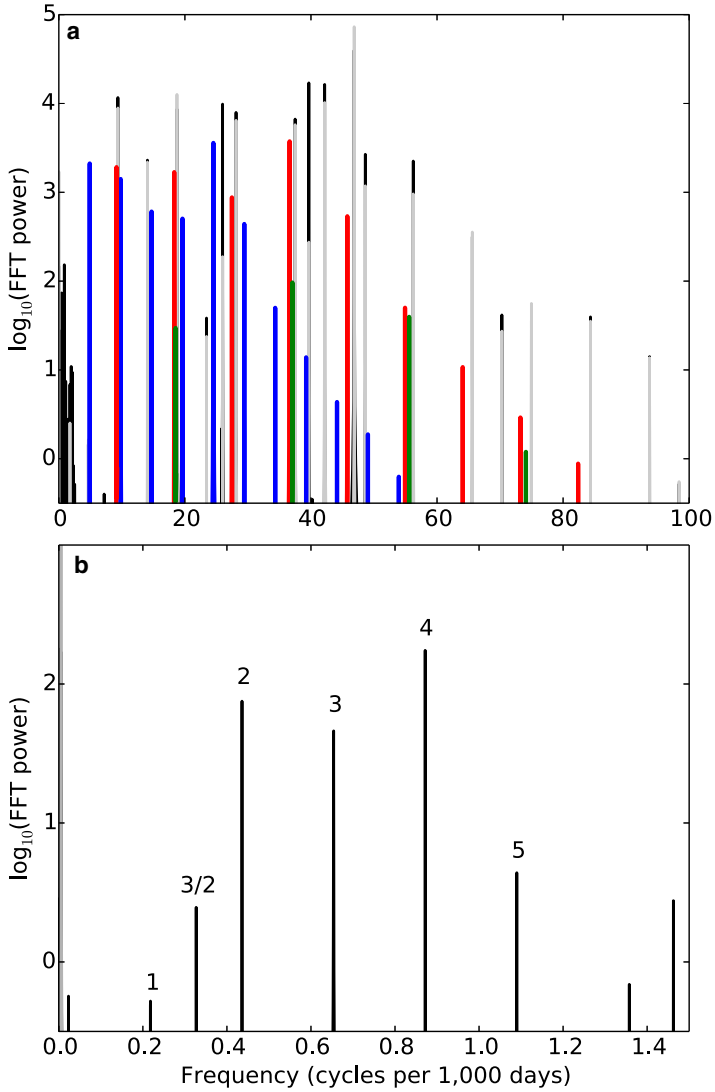

Extended Data Figure 3 | Spectral signatures of Kerberos. We merge Pluto and Charon into a single central body and integrate $\Phi(t)$ for Styx in exact resonance. The fast Fourier transform (FFT) power spectrum for $M_K = 0$ (light grey) obscures the same spectrum obtained when M_K is nominal. Unobscured spikes are caused by Kerberos. **a**, The impulses of Kerberos passing each moon create a signature at the synodic period and its overtones: $S_{SK} = 53.98$ days (green); $S_{NK} = 109.24$ days (red); $S_{KH} = 203.92$ days (blue). **b**, Harmonics of the second resonance, with period $42S_{NK} \approx 43S_{SN} \approx 4{,}590$ days, are also visible. The 3/2 harmonic is unexplained.

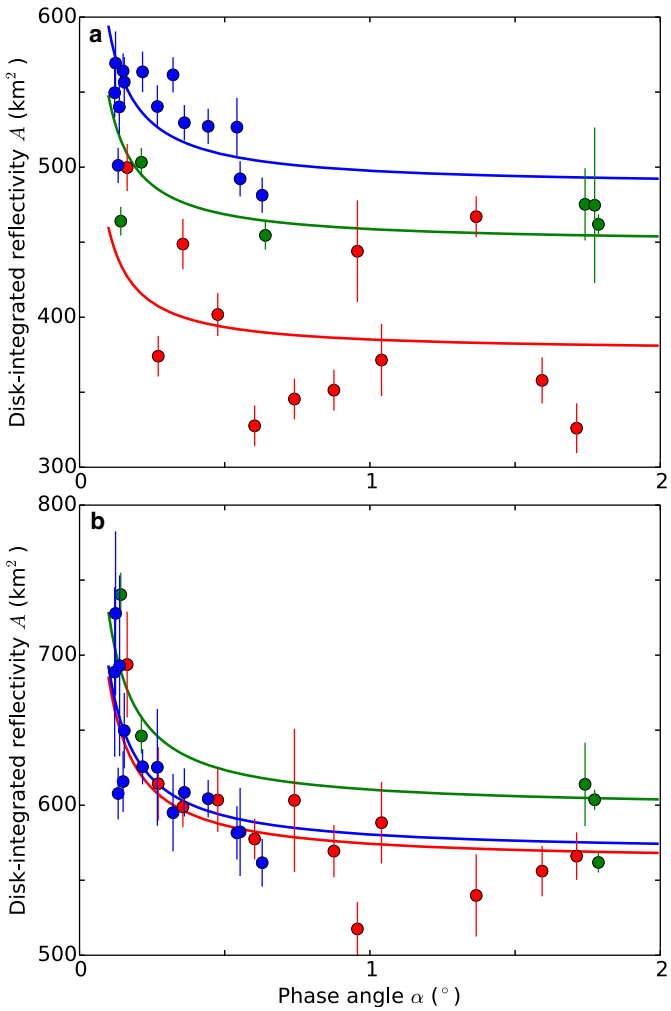

Extended Data Figure 4 | Satellite phase curves. Raw disk-integrated photometry has been plotted versus phase angle α for Nix (**a**) and Hydra (**b**). Vertical bars are $\pm 1\sigma$. An opposition surge is apparent. A simple parametric model for the phase curve is shown: $c(1 + d/\alpha)$, where d is fixed but c is scaled to fit each moon during each year. Measurements and curves are colour-coded by year: red for 2010, green for 2011, and blue for 2012.

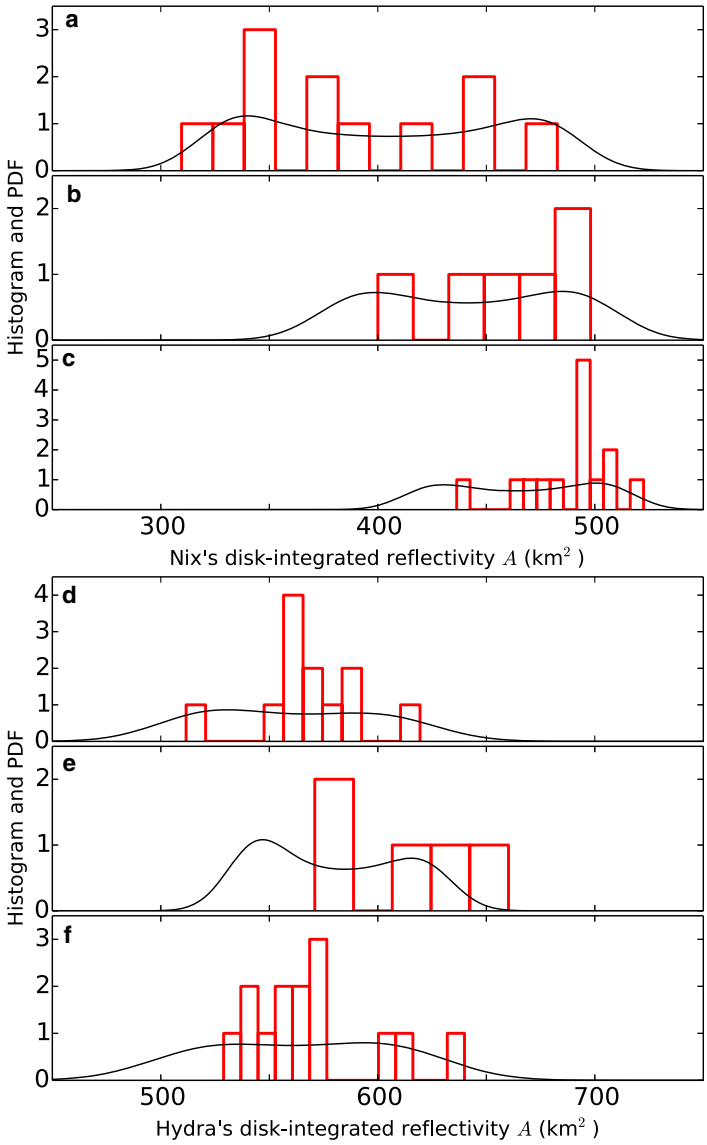

Extended Data Figure 5 | Distribution of photometric measurements by year. The black curves show the theoretical probability density function (PDF) of A by year for Nix (**a**, 2010; **b**, 2011; **c**, 2012) and Hydra (**d**, 2010; **e**, 2011; **f**, 2012), after convolution with the measurement uncertainties. The histogram of measurements from each year is shown in red. In spite of small number statistics, the measurements appear to be well described by the models, which have been derived via Bayesian analysis.

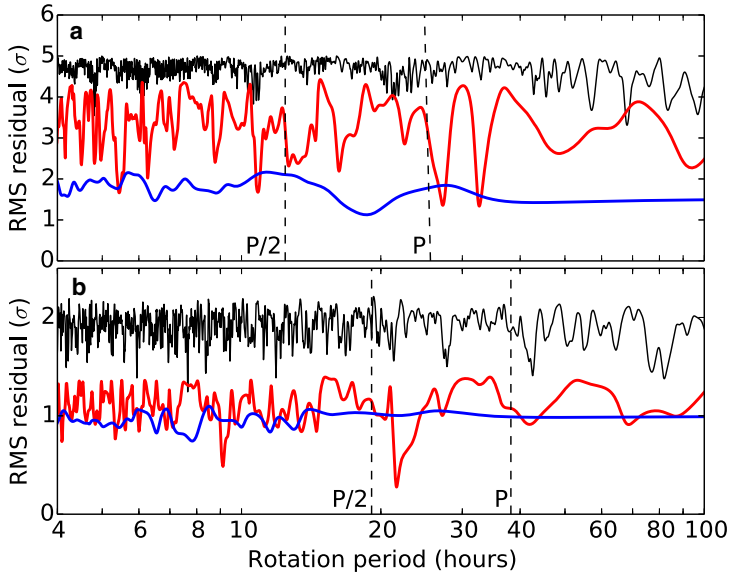

Extended Data Figure 6 | Searches for rotation periods in the light curves. We fitted a simple model involving a frequency and its first harmonic to the photometry (see equation (6)) of Nix (**a**) and Hydra (**b**). Curves are plotted for data from 2010 (red), 2012 (blue) and for three years 2010–2012 (black). Local minima with RMS residuals $\lesssim 1$ indicate a plausible fit. The orbital periods and half-periods are identified; if either moon were in synchronous rotation, we would expect to see minima near either P (for albedo variations) or $P/2$ (for irregular shapes).

Extended Data Table 1 | Orbital elements based on coupling various orbital elements and based on subsets of the data.

Moon	Years	N	a (km)	λ_0 (°)	n (°/day)	e (10^{-3})	ϖ_0 (°)	$\dot{\varpi}$ (°/day)	i (°)	Ω_0 (°)	$\dot{\Omega}$ (°/day)	P (days)	P/P_C	RMS (σ)	RMS (mas)	RMS (km)	M_1	M_0
Styx	**2006–2012**	**9**	42,662	276.8627	17.855814	5.892	296.15	0.49961	0.819	182.64	-0.50097	20.16150	3.156534	1.45	17.9	397	47	19
		±	81	0.0983	0.000255	1.179	9.49	0.02288	0.164	12.60	0.02376	0.00029	0.000050					
Styx	**2006–2012**	**8**	42,656	276.8562	17.855770	5.787	296.05	0.50581	0.809	183.36	-0.49187	20.16155	3.156542	1.44	17.8	397	47	19
		±	78	0.0955	0.000235	1.144	9.40	0.01405	0.162	12.50		0.00027	0.000046					
Styx	**2006–2012**	**7**	42,484	276.5918	17.855355	1.162	347.19	0.37688	0.381	176.10	-0.36908	20.16202	3.156615	1.79	19.3	429	47	19
		±	82	0.1046	0.000286	1.117	64.15		0.242	27.27		0.00032	0.000052					
Styx	**2006–2012**	**6**	42,422	276.5781	17.855333	1.054	7.70	0.37688	0.302	169.14	-0.36908	20.16204	3.156619	1.79	19.1	426	47	19
		±		0.1031	0.000285	1.102	65.26		0.215	33.76		0.00032	0.000052					
Styx	**2010**	**7**	43,549	239.9346	17.840396	7.733	138.44	0.37600	2.502	0.88	-0.36824	20.17892	3.159262	1.29	12.9	288	7	4
		±	617	0.2837	0.005338	2.225	16.61		0.894	13.64	0.00604	0.00604	0.000871					
Styx	**2011**	**3**	42,383	277.0515	17.807823								3.165041	1.10	16.1	363	12	1
		±		0.1879	0.018868								0.003818					
Styx	**2012**	**7**	42,856	332.3448	17.868293	6.915	116.85	0.37763	1.215	11.66	-0.36982	20.14742	3.154330	1.46	19.1	432	26	13
		±	117	0.2178	0.014056	1.712	11.95		0.297	13.73	0.01585	0.01585	0.003199					
Nix	**2006–2012**	**9**	48,697	63.8733	14.484221	2.022	220.27	0.19074	0.139	358.77	-0.15203	24.85463	3.891303	2.58	4.22	94	831	27
		±	3	0.0059	0.000015	0.050	1.41	0.00436	0.008	3.41	0.00842	0.00003	0.000004					
Nix	**2006–2012**	**8**	48,694	63.8655	14.484222	2.036	221.64	0.18325	0.133	3.73	-0.18096	24.85463	3.891302	2.59	4.25	95	831	27
		±	3	0.0056	0.000015	0.050	1.40	0.00409	0.008	3.40		0.00003	0.000004					
Nix	**2006–2012**	**7**	48,696	63.8580	14.484244	2.022	213.64	0.21395	0.133	15.03	-0.21084	24.85459	3.891296	2.65	4.35	97	831	27
		±	3	0.0054	0.000016	0.043	1.15		0.008	3.21	0.00003	0.00003	0.000004					
Nix	**2006–2012**	**6**	48,693	63.8573	14.484240	2.030	213.40	0.21395	0.132	13.88	-0.21084	24.85460	3.891297	2.65	4.35	97	831	27
		±		0.0054	0.000016	0.041	1.13		0.008	2.89		0.00003	0.000050					
Nix	**2010**	**7**	48,670	177.1349	14.483409	3.297	146.01	0.21392	0.070	319.59	-0.21080	24.85603	3.891521	2.17	4.41	99	85	2
		±	10	0.0158	0.000385	0.143	2.37		0.024	20.48	0.00066	0.00066	0.000100					
Nix	**2011**	**7**	48,670	63.8130	14.484954	1.598	229.57	0.21398	0.107	352.81	-0.21086	24.85338	3.891106	2.75	5.22	117	124	11
		±	8	0.0187	0.000346	0.123	4.32		0.023	13.89	0.00059	0.00059	0.000094					
Nix	**2012**	**7**	48,704	325.0999	14.481191	2.068	292.10	0.21383	0.163	302.70	-0.21072	24.85983	3.892117	2.35	3.71	84	613	14
		±	4	0.0067	0.000382	0.060	1.27		0.011	3.51	0.00066	0.00066	0.000101					
Kerberos	**2005–2012**	**9**	57,832	94.3375	11.191287	3.471	186.59	0.12121	0.356	241.86	-0.20985	32.16788	5.036283	1.27	11.2	248	185	32
		±	20	0.0206	0.000063	0.209	3.58	0.00795	0.037	5.48	0.01302	0.00018	0.000030					
Kerberos	**2005–2012**	**8**	57,783	94.3078	11.191398	3.280	187.64	0.11536	0.389	225.15	-0.11419	32.16756	5.036233	1.26	11.2	249	185	32
		±	19	0.0211	0.000050	0.200	3.74	0.00615	0.037	5.43		0.00014	0.000024					
Kerberos	**2005–2012**	**7**	57,781	94.3074	11.191394	3.272	187.28	0.10957	0.385	225.17	-0.10851	32.16757	5.036234	1.27	11.3	251	185	32
		±	19	0.0214	0.000050	0.203	3.75		0.037	5.54	0.00014	0.00014	0.000024					
Kerberos	**2005–2012**	**6**	57,750	94.3085	11.191397	3.221	187.86	0.10957	0.411	226.88	-0.10851	32.16756	5.036233	1.27	11.2	249	185	32
		±		0.0213	0.000050	0.199	3.79		0.035	4.86		0.00014	0.000024					
Kerberos	**2010**	**7**	57,825	329.5189	11.189590	4.877	140.09	0.10953	0.284	298.05	-0.10846	32.17276	5.037046	1.24	8.78	196	30	10
		±	48	0.0542	0.001181	0.481	5.69		0.090	17.99	0.00340	0.00340	0.000561					
Kerberos	**2011**	**7**	57,776	94.1883	11.194672	1.890	216.87	0.10965	0.515	250.03	-0.10859	32.15815	5.034760	1.19	6.99	157	30	1
		±	40	0.0680	0.001446	0.497	14.19		0.084	8.23	0.00415	0.00415	0.000652					
Kerberos	**2012**	**7**	57,803	230.3510	11.190758	3.335	233.57	0.10955	0.434	172.29	-0.10849	32.16940	5.036521	1.24	12.28	278	119	20
		±	38	0.0418	0.004783	0.423	8.24		0.074	10.08	0.01375	0.01375	0.002352					
Hydra	**2006–2012**	**9**	64,741	197.8685	9.423633	5.837	192.40	0.06842	0.244	191.15	-0.08762	38.20183	5.980972	2.73	3.19	71	835	24
		±	3	0.0032	0.000009	0.025	0.26	0.00081	0.005	1.19	0.00317	0.00003	0.000005					
Hydra	**2006–2012**	**8**	64,738	197.8662	9.423647	5.862	192.22	0.06986	0.242	189.67	-0.06934	38.20177	5.980963	2.77	3.21	72	835	24
		±	3	0.0032	0.000008	0.025	0.27	0.00080	0.005	1.17		0.00003	0.000005					
Hydra	**2006–2012**	**7**	64,738	197.8664	9.423645	5.861	192.04	0.07101	0.242	189.91	-0.07048	38.20178	5.980965	2.77	3.22	72	835	24
		±	3	0.0032	0.000008	0.025	0.24		0.005	1.15	0.00003	0.00003	0.000005					
Hydra	**2006–2012**	**6**	64,721	197.8691	9.423638	5.881	192.04	0.07101	0.249	193.12	-0.07048	38.20181	5.980969	2.80	3.25	72	835	24
		±		0.0032	0.000008	0.025	0.24		0.005	0.99		0.00003	0.000005					
Hydra	**2010**	**7**	64,730	358.2681	9.423299	6.661	165.04	0.07101	0.334	219.90	-0.07048	38.20318	5.981184	2.77	3.07	69	85	2
		±	8	0.0079	0.000199	0.080	0.63		0.013	2.25	0.00081	0.00081	0.000124					
Hydra	**2011**	**7**	64,746	197.8686	9.423495	5.722	192.77	0.07101	0.242	193.93	-0.07048	38.20239	5.981060	2.88	3.24	73	135	12
		±	12	0.0166	0.000157	0.271	2.13		0.030	4.77	0.00064	0.00064	0.000088					
Hydra	**2012**	**7**	64,739	46.9262	9.422786	5.763	218.15	0.07100	0.214	157.81	-0.07047	38.20526	5.981510	2.35	2.93	66	606	10
		±	3	0.0033	0.000592	0.050	0.43		0.006	1.91	0.00240	0.00240	0.000379					

Columns M_1 and M_0 identify the numbers of measurements included in and excluded from the fit; N indicates the number of free parameters. When $N = 8$, we derived $\dot{\Omega}$ from the relationship $\nu^2 = 2n^2 - \kappa^2$. For $N = 7$, $\dot{\varpi}$ and $\dot{\Omega}$ were both derived from n and the gravity field using equations (5b) and (5c). For $N = 6$, a was also coupled to n via equation (5a). $N = 3$ indicates a fit to a circular orbit. For fits to single years of data, the epoch is 1 July UTC for that year. We disfavour $N \leq 7$ in the multi-year fits because some residuals increase markedly.